

Contents lists available at ScienceDirect

### Ultramicroscopy

journal homepage: www.elsevier.com/locate/ultramic





## Angstrom-scale imaging of magnetization in antiferromagnetic $Fe_2As$ via 4D-STEM

Kayla X. Nguyen <sup>a,1</sup>, Jeffrey Huang <sup>a,1</sup>, Manohar H. Karigerasi <sup>a</sup>, Kisung Kang <sup>a</sup>, David G. Cahill <sup>a,b</sup>, Jian-Min Zuo <sup>a,b</sup>, André Schleife <sup>a,b,c</sup>, Daniel P. Shoemaker <sup>a,b</sup>, Pinshane Y. Huang <sup>a,b,\*</sup>

- <sup>a</sup> Department of Materials Science and Engineering, University of Illinois Urbana-Champaign, Urbana, IL 61801, United States
- <sup>b</sup> Materials Research Laboratory, University of Illinois Urbana-Champaign, Urbana, IL 61801, United States
- c National Center for Supercomputing Applications, University of Illinois Urbana-Champaign, Urbana, IL 61801, United States

#### ARTICLE INFO

# Keywords: Antiferromagnetism 4D-STEM $Fe_2As$ Magnetic imaging

#### ABSTRACT

We demonstrate a combination of computational tools and experimental 4D-STEM methods to image the local magnetic moment in antiferromagnetic  $Fe_2As$  with 6 angstrom spatial resolution. Our techniques utilize magnetic diffraction peaks, common in antiferromagnetic materials, to create imaging modes that directly visualize the magnetic lattice. Using this approach, we show that center-of-mass analysis can determine the local magnetization component in the plane perpendicular to the path of the electron beam. Moreover, we develop Magnstem, a quantum mechanical electron scattering simulation code, to model electron scattering of an angstrom-scale probe from magnetic materials. Using these tools, we identify optimal experimental conditions for separating weak magnetic signals from the much stronger interactions of an angstrom-scale probe with electrostatic potentials. Our techniques should be useful for characterizing the local magnetic order in systems such in thin films, interfaces, and domain boundaries of antiferromagnetic materials, which are difficult to probe with existing methods.

#### 1. Introduction

For decades, transmission electron microscopy (TEM) and scanning TEM (STEM) methods such as Lorentz TEM, electron holography, and differential phase contrast (DPC) have provided valuable insight into the magnetic structure of materials on the micro and nanoscales. The relatively high spatial resolution of these methods, which is typically 5–20 nanometers (nm), but can reach up to around 1 nm [1], have made them valuable for uncovering variations in the local magnetization such as domain walls in ferromagnets, skyrmions, and the magnetization of nanoparticles and thin films. As TEM-based techniques continue to improve, a natural question is whether electron microscopy techniques can be extended to probe local magnetization on the atomic scale.

Antiferromagnets such as  $Fe_2As$  (Fig. 1b) have received renewed interest as potential materials to increase the speed and density of spintronic devices because they exhibit terahertz spin dynamics, have low magnetic susceptibility, and lack stray fields. Because their local magnetization varies periodically on the scale of a few angstroms, antiferromagnets offer ideal systems to test methods for atomic scale magnetic characterization. New TEM-based magnetic imaging techniques could directly probe magnetic ordering in antiferromagnets in

real space, complementing bulk characterization methods such as neutron diffraction [2], while also achieving the high spatial resolution of surface sensitive techniques such as spin-polarized scanning tunneling microscopy [3].

Yet, few TEM studies have been attempted to image antiferromagnetic order. Part of the challenge is spatial resolution: a few-nanometer electron beam would average over several magnetic unit cells in most antiferromagnets, producing no net magnetic deflection. Sensitivity is another: for techniques such as DPC that detect magnetization as a deflection of the electron beam, the minimum detectable deflection is inversely proportional to probe size [4,5]. This trade-off between spatial resolution and sensitivity to magnetic fields makes it difficult to detect magnetic signals at atomic length scales. A third and particularly insidious challenge for electron microscopy is that magnetization in antiferromagnets varies on the same length scale as the atomic spacings in materials, making it exceptionally difficult to isolate magnetic signals from scattering effects from the crystallographic lattice. Recently, DPC-STEM has been used to probe antiferromagnetism across a domain wall [6] and, via kernel filtering and unit-cell averaging, has recently been used to map the magnetic structure of an antiferromagnet in real

<sup>\*</sup> Corresponding author at: Materials Research Laboratory, University of Illinois Urbana-Champaign, Urbana, IL 61801, United States. E-mail address: pyhuang@illinois.edu (P.Y. Huang).

<sup>&</sup>lt;sup>1</sup> Contributed equally to this work.

K.X. Nguyen et al. Ultramicroscopy 247 (2023) 113696

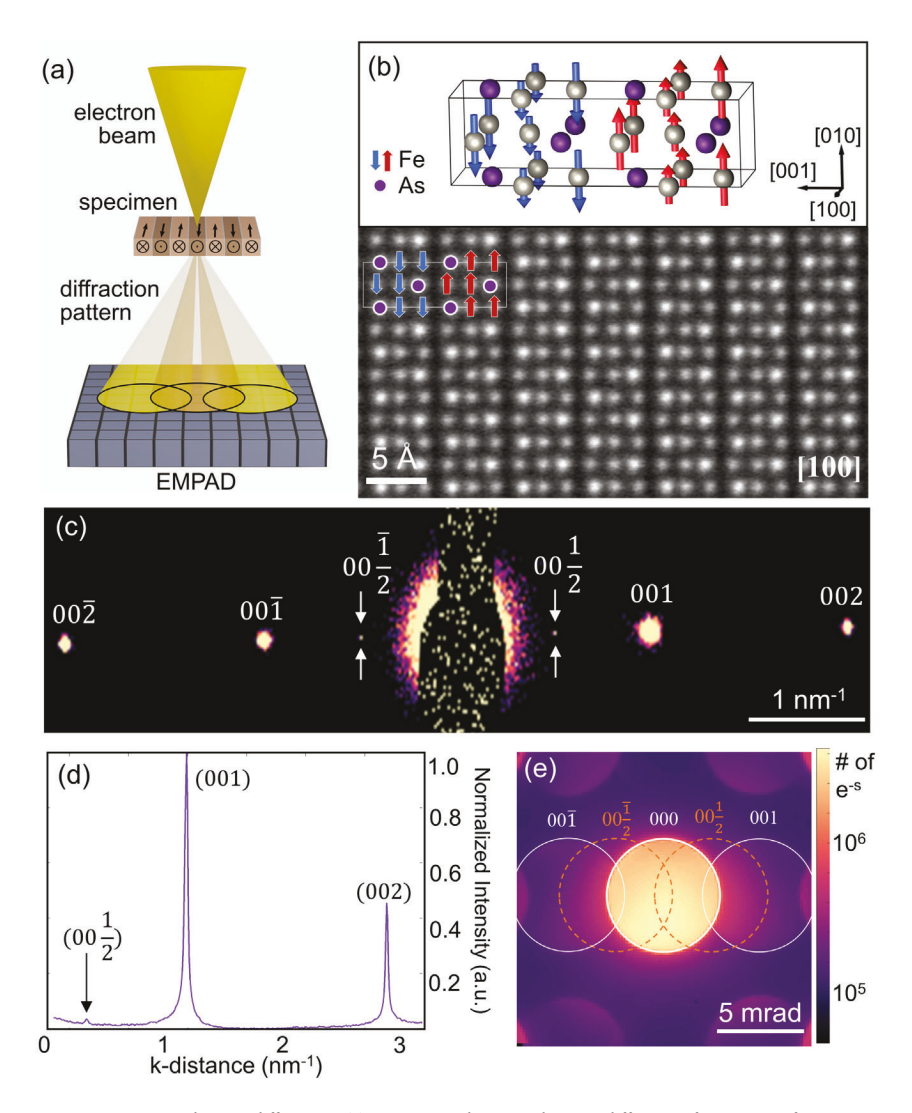


Fig. 1. Detecting antiferromagnetism in Fe<sub>2</sub>As using electron diffraction. (a) 4D-STEM schematic showing diffraction from an antiferromagnet with an angstrom-size probe. (b) Magnetic unit cell (top) and atomic resolution ADF-STEM image (bottom) of Fe<sub>2</sub>As. Arrows indicate directions of Fe magnetic moments. (c) TEM diffraction pattern showing weak magnetic  $\left\{00\frac{1}{2}\right\}$  spots. The complete diffraction pattern is shown in Figure S1. (d) Line profile of (c), showing the relative intensity of each peak. (e) CBED pattern captured in 4D-STEM with circles indicating diffracted disks.

space [7]. However, these methods remain somewhat indirect, and the detection mechanisms behind these recent observations and how magnetic signals can be reliably separated from atomic structure remain unclear. By collecting the full diffraction pattern, four-dimensional (4D) STEM studies can provide greater measurement flexibility and insight into the effect of magnetism on electron scattering. Here, we use the latest generation of direct electron detectors for 4D-STEM, combined with electron scattering simulations to model, measure, and extract the local magnetization on the few-angstrom scale.

#### 2. Results and discussion

We demonstrate our approach on Fe<sub>2</sub>As, a collinear, metallic antiferromagnet with a Néel temperature of 353 K. Fig. 1b shows the structure of Fe<sub>2</sub>As: it has a tetragonal crystal structure (a=3.63 Å, c=5.98 Å) [8]. The Néel vector for Fe<sub>2</sub>As can lie along either of the crystallographically equivalent a or b axes, and the magnetic unit cell has dimensions  $a \times a \times 2c$ . Single crystals of Fe<sub>2</sub>As were grown by slow-cooling stoichiometric mixtures of the elements from the melt at 1000 °C in fused silica ampoules, following the detailed procedure in Ref. [9]. Then, TEM specimens of Fe<sub>2</sub>As were prepared using standard focused ion beam lift-out procedures and imaged with aberration-corrected STEM. Fig. 1b shows an annular dark-field STEM image of

 ${\rm Fe_2As}$  along the [100] zone axis. In this orientation, vertical blocks three atoms wide, or "trilayers" are visible. Within each 6 Å-wide trilayer, the magnetic moments of the Fe atoms are aligned parallel, while the magnetic moments of adjacent trilayers are antiparallel.

#### 2.1. Selected area electron diffraction

We first confirm that antiferromagnetic ordering can be detected in our sample. Fig. 1c shows a room temperature selected area electron diffraction (SAED) pattern of Fe<sub>2</sub>As along the [100] zone (see full diffraction pattern in Figure S1). While the brightest peaks in the diffraction pattern arise from Bragg diffraction from the crystal, we also observe weak diffraction spots (white arrows in Fig. 1c) with an intensity of roughly 1/20 to 1/300 of the {001} diffraction spots (Fig. 1d), depending on the region and sample thickness measured. These magnetic  $\left\{00\frac{1}{2}\right\}$  diffraction peaks correspond to the 2c length of the magnetic unit cell. Similar half-order peaks have been previously observed in electron beam diffraction of antiferromagnetic NiO [10], and magnetic diffraction peaks with fractional k-vectors are also routinely observed in neutron diffraction studies of antiferromagnets, where they are used to determine magnetic structures. Importantly, the presence of the  $\left\{00\frac{1}{2}\right\}$  spots in the SAED pattern

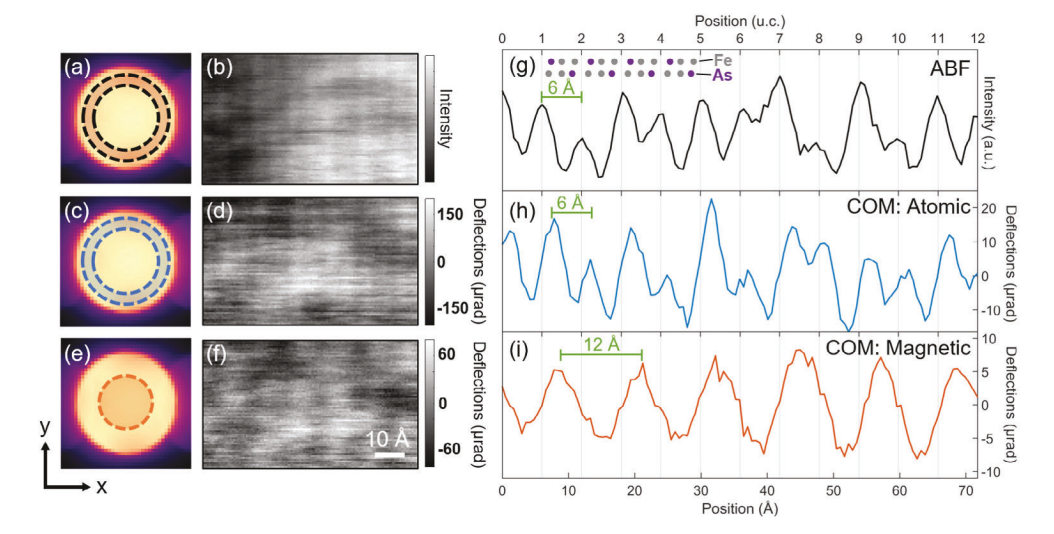


Fig. 2. Separating structural and magnetic lattices via COM imaging. Virtual ABF and COM images from experimental 4D-STEM data, acquired using an electron beam with 3.5 mrad semi-convergence angle at 120 kV, over  $120 \times 71$  probe positions with a spacing of 0.61 Å per pixel. Diffraction patterns and virtual images are oriented with the c axis pointing in the x-direction and an a axis pointing in the y-direction. (a) An annular virtual detector is used to reconstruct (b) an annular bright field (ABF) image. Integrating over (c) the same annular region as (b), (d) an x-component center of mass (COMx) image showing atomic contrast is formed. Integrating over (e) a small circular region within the BF disk to form (f) a COMx image showing magnetic contrast. (g-x) Background-subtracted line profiles of the images (b), (d), and (f). The overlay in (g) shows the atomic structure of Fe<sub>2</sub>As. COMx deflections due to magnetic contrast have a spatial period twice that of the atomic contrast, consistent with the structure of Fe<sub>2</sub>As. Line profiles were obtained by averaging along the (001) lattice fringes seen in Fig. 2(b) to mitigate the effects of scan distortion.

demonstrates that antiferromagnetic ordering is detectable in our  ${\rm Fe_2As}$  sample.

#### 2.2. Experimental 4D-STEM

Next, we extend our measurements to the atomic scale using 4D-STEM. In 4D-STEM, an angstrom to nanoscale electron beam is rastered across a sample, and a convergent beam electron diffraction (CBED) pattern is collected at each scan position (Fig. 1a). When combined with a new generation of fast, high-dynamic range direct electron detectors, 4D-STEM offers new opportunities to probe the structure and functional properties of materials at the atomic scale. A key advantage of 4D-STEM is that it collects the two-dimensional (2D) electron scattering distribution as a function of position, offering atomic-scale resolution while also providing more flexibility to extract and isolate signals of interest. This property has enabled measurements of angstrom-scale electrostatic fields, such as the local polarization of ferroelectrics [11–13] as well as nanoscale mapping of magnetic fields [5].

To acquire our 4D-STEM data, we used a Thermo Fisher Titan equipped with an electron microscope pixel array detector (EMPAD), a 128 × 128 pixel direct electron detector with a high dynamic range of 1,000,000:1 [14]. This high dynamic range allows us to achieve high signal-to-noise ratios and detect small intensity changes from magnetism [5]. We used an acceleration voltage of 120 kilovolts (kV) and a semi-convergence angle of 3.5 milliradians (mrad), yielding a probe size of approximately 6 Å. This probe size was chosen to approximately match the width of the trilayers and the length scale of magnetization variations in our specimen. As we discuss later, this convergence angle maximizes the magnetic signal. We also operated with the objective lens on, rather than in a Lorentz or field-free mode. In this mode, the objective lens produces a magnetic field of 1.61 T normal to the sample plane, which should orient the Fe2As moments in-plane, perpendicular to the beam direction [15]. We calibrated the strength of the objective lens using Hall probe measurements reported in Ref. [5]. Fig. 1e shows a position averaged CBED pattern of Fe<sub>2</sub>As along the [100] zone axis captured using 4D-STEM. The CBED pattern contains similar information to the SAED pattern in Fig. 1c, but the use of a convergent beam results in the formation of diffraction disks, rather than spots. As we show below, while the magnetic  $\{00\frac{1}{2}\}$  reflections are too weak to be directly visible in the CBED pattern (Fig. 1e), they nevertheless produce measurable signals that enable atomic scale magnetic imaging.

In Fig. 2, we extracted three signals of interest from a 4D-STEM dataset. First, we created a virtual annular bright field (ABF) image by applying a digital mask (Fig. 2a) to each CBED pattern and integrating the counts within the virtual detector at each scan position. The resulting image (Fig. 2b) is similar to that generated by a conventional physical ABF STEM detector; dark vertical lines correspond to the locations of trilayers. Compared to the ADF STEM image in Fig. 1b, the contrast in the virtual ABF image is inverted because of the different choice of collection angles and the image resolution is decreased due to the relatively large 6 Å probe size.

In Fig. 2c–f, we apply center-of-mass (COM) analysis to our 4D-STEM data to separate and isolate signals from the crystal lattice and magnetic structure. COM analysis measures the center of mass of the intensity of the diffraction patterns acquired via 4D-STEM. When applied to the full diffraction pattern, the COM measures changes to the average momentum of the electron beam produced by its interactions with the specimen; correspondingly, COM analysis is commonly used to measure electric fields and magnetic domains [5,16,17]. In addition, application of COM analysis to selected regions of the CBED pattern has been shown to be an effective method to separate scattering phenomena that dominate different regions of reciprocal space [5].

While the COM is a 2D vector quantity, we focus here on a single component, COM shifts along the c-axis direction, since we expect that both the electrostatic and magnetic fields of Fe<sub>2</sub>As will produce COM deflections along this direction. Orienting the real space images and diffraction pattern so that the c axis points in the x-direction, we calculate the COMx shifts in regions of the diffraction pattern defined by the masks shown in Fig. 2c,e, creating the COM images in Fig. 2d,f. Fig. 2gi show background subtracted line profiles of the virtual ABF (Fig. 2g) and two COM images (Fig. 2h,i). Both the ABF line profile in Fig. 2g and the COM data in Fig. 2h reveal lattice fringes with the 6 Å periodicity of the trilayers of the structural unit cell. The COM signal in Fig. 2i is especially interesting: it alternates in direction from one trilayer to the next, and exhibits a 12 Å periodicity. As we show in Figure S3, these fringes can also be detected using DPC imaging using a virtual quadrant detector. The position and frequency of this COM signal are an excellent match for the local magnetization changes expected for antiferromagnetic Fe<sub>2</sub>As, a strong indicator that our data represents an experimental detection of the atomic scale antiferromagnetic ordering.

K.X. Nguyen et al. Ultramicroscopy 247 (2023) 113696

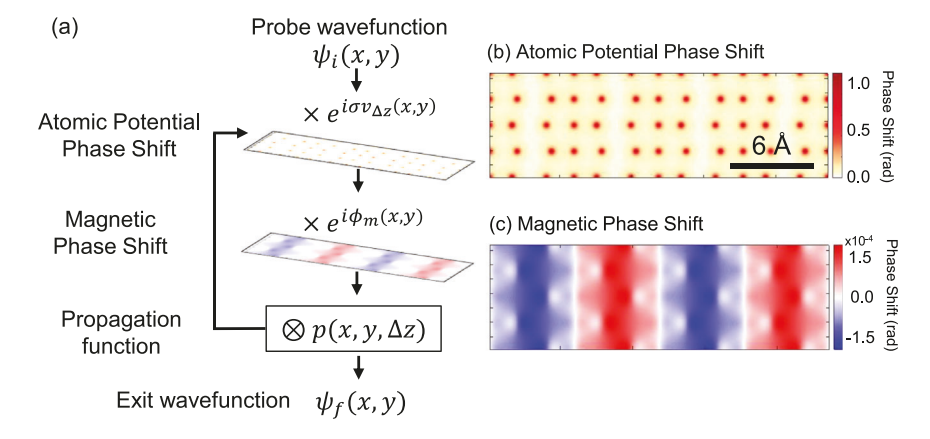


Fig. 3. Schematic of the Magnstem approach for electron scattering simulations in magnetic specimens: (a) The multislice method is modified to use a transmission function consisting of two phase shifts to model scattering through each atomic layer: a phase shift due to atomic potentials and a magnetic phase shift. (b) Phase shift due to projected atomic potentials and (c) phase shift due to projected magnetic fields shown for a one-unit-cell thick region of [100] Fe<sub>2</sub>As. As the probe wavefunction travels through the simulated sample, it receives a phase shift and is convolved with the propagation function at each slice of the sample.

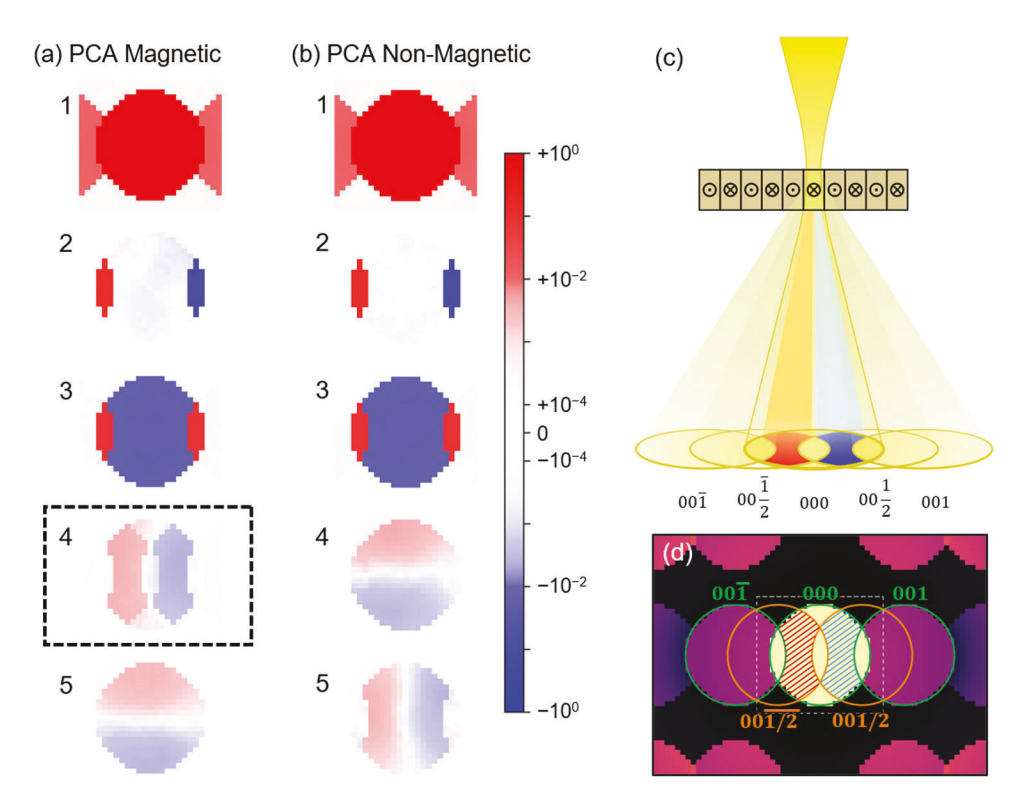


Fig. 4. Principal component analysis of electron scattering simulations shows unique principal component from magnetism. (a, b) The five largest principal components of the CBED patterns of a simulated 4D-STEM data set with magnetism (a) turned on or (b) turned off. The principal components are scaled by their singular values and arranged in descending order by size. The fourth component from the magnetic simulation results from the magnetic lattice, and its symmetry corresponds to the overlap between the direct beam and  $\left\{00\frac{1}{2}\right\}$  disks. (c) Schematic of the impact of the magnetic PCA component on the 4D-STEM signal. (d) Simulated PACBED pattern where the  $\left\{001\right\}$  disks are outlined in green and  $\left\{00\frac{1}{2}\right\}$  disks are outlined in orange. The expected asymmetry from magnetism can be observed in the BF disk within the overlap region of the  $\left\{00\frac{1}{2}\right\}$  disks (red and blue hatched areas). The region of the CBED patterns used in PCA analysis is indicated by the white dashed rectangle.

#### 2.3. 4D-STEM simulations using Magnstem

To understand the origins of these signals, we developed Magnstem, a quantitative simulation code to model the electron scattering of an angstrom-scale probe in magnetic materials. We based our methods on multislice [18], a powerful approach for simulating TEM experiments and calculating the dynamic scattering of the electron beam from electrostatic fields in the specimen. In multislice, the sample is divided into thin slices and the electron wave function is alternately scattered by the transmission function of a slice and propagated towards the next slice, as shown in Fig. 3a. While multislice simulations typically focus

only on scattering from the screened nuclear potential, a few groups have adapted multislice codes to incorporate scattering from magnetic fields [19–22].

In Magnstem, we describe the evolution of the probe wavefunction as follows:

$$\frac{\partial \psi(\mathbf{r})}{\partial z} = \left[ \frac{i}{2k} \nabla_{xy}^2 + i \left( \frac{me}{\hbar^2 k} V(\mathbf{r}) - \frac{e}{\hbar} A_z(\mathbf{r}) \right) \right] \psi(\mathbf{r}). \tag{1}$$

Here, the effect of magnetic fields within the plane of the sample enters through the component of the vector potential along the propagation direction  $A_z$ . We retain only the  $A_z$  term from the full paraxial Pauli

equation for a magnetic sample (Eq. (3) in Ref. [21]) because this term is two orders of magnitude larger than other terms that describe the interaction between electrons and magnetic fields when the spins are oriented perpendicular to the electron beam (see the Supplementary Material). Eq. (1) can then be modeled using the conventional multislice method using the following transmission function for a slice of the sample,

$$t(x, y, z) = \exp\left[i \int_{z}^{z+\Delta z} \left(\sigma V(x, y, z') - \frac{e}{\hbar} A_{z}(x, y, z')\right) dz'\right] \tag{2}$$

where  $\sigma = me/\hbar^2 k$ .

To implement this method, we modified the Kirkland multislice code [23], adding a contribution to the transmission function due to  $A_z$  (shown in Fig. 3c), which we derived from magnetization densities calculated for Fe<sub>2</sub>As using density-functional theory [9] (see the Supplementary Material). Magnstem adds to conventional multislice, where the electron beam undergoes phase shifts due to scattering from atomic potentials (Fig. 3b), by incorporating an additional phase shift due to the in-plane magnetic moments of the sample (Fig. 3c). As Fig. 3b—c show, the additional phase shift due to magnetic moments is small: 1000 to 10,000 times smaller than the phase shift due to atomic moments

We next use Magnstem to simulate 4D-STEM datasets, matching key parameters of simulation to experiment (see the Supplementary Material). We simulate  $Fe_2As$  down the [100] direction with a thickness of 9.1 nm (25 unit cells), creating a 4D dataset by rastering the simulated probe over  $15 \times 45$  probe positions, saving the CBED pattern at each probe position. To account for atomic vibrations, the frozen phonon approximation was employed [24], with each CBED pattern averaged over 10 frozen phonon configurations. We note that this approach is distinct from the finite difference technique to compute phonon properties of materials from first-principles [25], sometimes also referred to as frozen-phonon method. To isolate the impact of antiferromagnetism on electron scattering, we conducted two sets of 4D-STEM simulations with the magnetism turned either on or off, then used principal component analysis (PCA) to analyze the resulting CBED patterns (Fig. 4).

Fig. 4a–b show the principal components for the two 4D-STEM data sets. Comparing the magnetic and non-magnetic simulations, the first three principal components and their corresponding real-space maps are nearly identical, indicating they arise primarily from the atomic lattice of the material (see Figure S4 for PCA components, singular values, and corresponding real space maps). Accordingly, real space maps of the first three PCA components (Figure S4) each produce (001) lattice fringes with the 6 Å periodicity of the crystallographic unit cell.

Notably, we find that the fourth PCA component of the magnetic simulations (Fig. 4a, black dashed box) provides the basis for angstrom-scale STEM imaging of antiferromagnetism. The shape and symmetry of this component, which is absent in the non-magnetic simulations, corresponds to regions of overlap between the BF disk and the magnetic  $\left\{00\frac{1}{2}\right\}$  disks (Fig. 4c–d). In addition, real space maps for this component (Figure S4) show  $\left(00\frac{1}{2}\right)$  lattice fringes with the 12 Å periodicity of the magnetic unit cell.

These results are important because they explain the physical origin behind angstrom-scale detection of antiferromagnetism and illustrate how to set up direct imaging modes for magnetic lattice fringes. In short, the periodic magnetic structure of Fe<sub>2</sub>As acts as a weak phase grating, producing  $\left\{00\frac{1}{2}\right\}$  disks. When these magnetic reflections overlap with the direct beam, they produce magnetic lattice fringes—a direct parallel to how overlap between structural Bragg disks gives rise to structural lattice fringes. Notably, this mechanism is distinct from the conventional mechanisms used to explain Lorentz TEM and STEM signals for ferromagnetic materials, where slowly varying magnetic fields produce rigid shifts of the entire diffraction pattern. The semi-convergence angle has a strong impact on the interpretability and

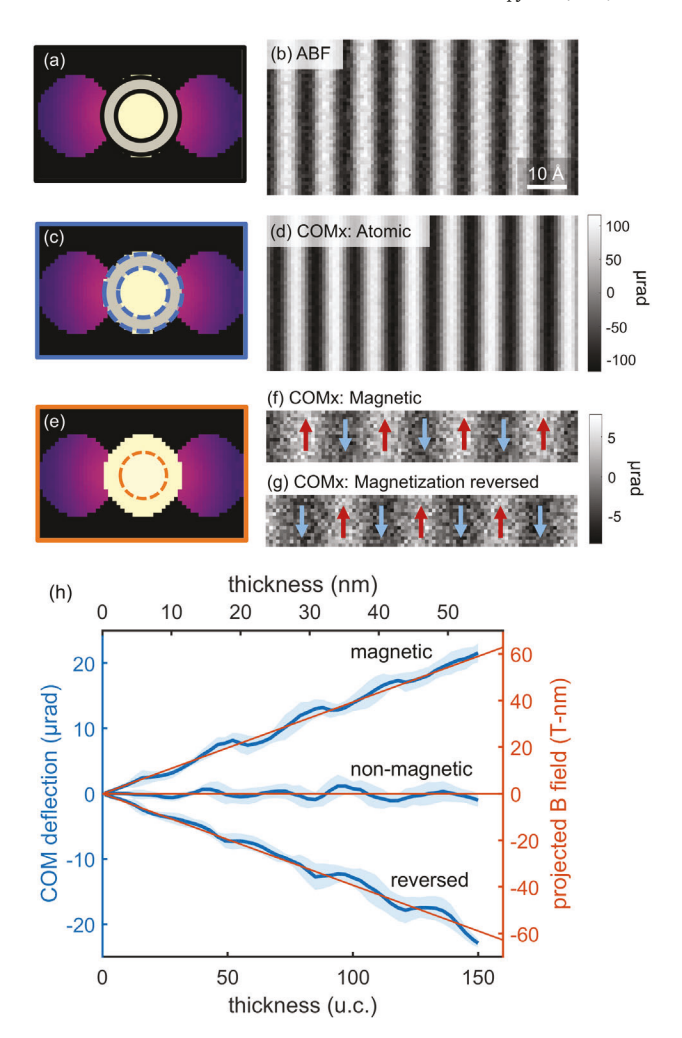


Fig. 5. Center-of-mass imaging in simulated 4D-STEM data. (a) An annular virtual detector, shown overlaid over a simulated CBED pattern, is used to reconstruct (b) an ABF image. (c–g) Two images mapping the x-direction shifts in the center of mass (COMx) were constructed, using either (c–d) an annular region which overlaps with the  $\{001\}$  disks or (e–g) a small circular region that overlaps with the  $\{00\frac{1}{2}\}$  disks. (f–g) In (g), the magnetic moments were reversed in direction compared to (f). The contrast in (g) is opposite that of (f), indicating that the direction of the in-plane magnetic moment can be uniquely determined. The ABF and COMx images were tiled to emphasize the spatial periodicity of the fringes. (h) COMx deflection (blue) as a function of sample thickness, for simulated thicknesses up to 150 unit cells. COMx deflection values were averaged over 8 probe positions along the middle of a trilayer; the standard deviation from those probe positions is shown as blue shading.

strength of the magnetic signal. We show using Magnstem simulations (Figure S5) that the magnetic signals are strongest when the probe size is approximately 6 Å wide, matching the length scale of the magnetic columns in the sample. This can also be understood in terms of the diffraction pattern: magnetic contrast arises from overlap of the magnetic disks with the BF disk, and this probe size maximizes that overlap (Figure S6).

Finally, we performed COM analyses of the 4D-STEM simulations, mirroring the processing approach used for experimental data. Unlike in simulations, we found that a simple PCA analysis was not sufficient to isolate the magnetic signal in experimental data. This is likely because CBED patterns from experimental samples contain spatially-varying components due to sample preparation and beam damage making it difficult to isolate the weaker magnetic contributions in the CBED patterns. Overall, our simulations are an excellent match for the experimental data in Fig. 2. In contrast to PCA, we found COM imaging using selected regions of the BF disk to be a robust approach for

K.X. Nguyen et al. Ultramicroscopy 247 (2023) 113696

isolating magnetism in both experiment and simulations. Moreover, we show in Fig. 5f–g that COM analysis can unambiguously determine the sign of the in-plane component of magnetic moment (for example, the up vs. down arrows in Fig. 5f). This ability arises from the asymmetry of the phase between the  $\left\{00\frac{1}{2}\right\}$  peaks and the corresponding intensity asymmetry of the magnetic PCA component in Fig. 4.

In TEM imaging of crystalline samples, lattice fringes arising from the atomic structure have been observed to reverse in contrast as the sample thickness changes. Thus, proper interpretation of the magnetic signal requires understanding how it scales with sample thickness. We simulated 4D-STEM data sets over a range of thicknesses, from 0.36 nm to 54.3 nm (Fig. 5h) and measured the intensity of magnetism-induced COM shifts in the overlap region (Fig. 5e). Fig. 5h shows that the COMx signal increases approximately linearly with the sample thickness and projected magnetic field. These results show that it is advantageous to use a thicker specimen to maximize the magnetic signal, without potential complications from contrast reversal.

#### 3. Conclusions

In summary, we developed an approach for imaging the magnetic structure of antiferromagnets in real space using 4D-STEM. In our work, to increase the signal from the magnetic structure, we match the size of the electron probe to the size of regions of aligned spins. Using Magnstem simulations, we observe that the periodic magnetic structure of Fe<sub>2</sub>As redistributes intensity in CBED patterns at the overlap of antiferromagnetic  $\left\{00\frac{1}{2}\right\}$  disks with the BF disk. By selecting those regions within the BF disk, COM imaging can be used to detect the magnetic structure of Fe<sub>2</sub>As. This approach can be broadly applied to antiferromagnets whose magnetic structures produce fractional antiferromagnetic reflections, and should allow for the determination of magnetic structure in antiferromagnetic thin films and imaging of antiferromagnetic domains, antiphase boundaries, and domain walls.

#### Declaration of competing interest

The authors declare the following financial interests/personal relationships which may be considered as potential competing interests: KXN is a co-inventor on the license for the EMPAD detector to Thermo Fisher Scientific.

#### Data availability

Data will be made available on request.

#### Acknowledgments

The authors thank D. A. Muller for useful discussions. This work was supported by the Air Force Office of Scientific Research, United States under award number FA9550-20-1-0302. K.X.N. is also supported in part by the L'Oreal For Women in Science Postdoctoral Fellowship, United States. J.H. is partially supported by the DIGI-MAT program through National Science Foundation, United States under Grant No. 1922758. Electron microscopy facilities were provided by the University of Illinois Materials Research Laboratory and the Cornell Center for Materials Research through the National Science Foundation MRSEC program, United States through award DMR-1719875. The crystal growth and density functional calculations were supported by the Illinois Materials Research Science and Engineering Center through the National Science Foundation MRSEC program, United States, award DMR-1720633. This work made use of the Illinois Campus Cluster, a computing resource that is operated by the Illinois Campus Cluster Program (ICCP) in conjunction with the National Center for Supercomputing Applications (NCSA) and which is supported by funds from the University of Illinois at Urbana-Champaign, United States.

#### Appendix A. Supplementary data

Supplementary material related to this article can be found online at https://doi.org/10.1016/j.ultramic.2023.113696.

#### References

- [1] V. Boureau, M. Staňo, J.-L. Rouvière, J.-C. Toussaint, O. Fruchart, D. Cooper, High-sensitivity mapping of magnetic induction fields with nanometer-scale resolution: comparison of off-axis electron holography and pixelated differential phase contrast, J. Phys. D: Appl. Phys. 54 (2021) 085001, http://dx. doi.org/10.1088/1361-6463/abc77d, https://iopscience.iop.org/article/10.1088/ 1361-6463/abc77d.
- M. Schlenker, J. Baruchel, Possibilities of X-ray and neutron topography for domain and phase coexistence observations, Ferroelectrics 162 (1) (1994) 299–306, http://dx.doi.org/10.1080/00150199408245118.
- [3] M. Enayat, Z. Sun, U.R. Singh, R. Aluru, S. Schmaus, A. Yaresko, Y. Liu, C. Lin, V. Tsurkan, A. Loidl, J. Deisenhofer, P. Wahl, Real-space imaging of the atomic-scale magnetic structure of Fe<sub>1+y</sub>Te, Science 345 (6197) (2014) 653–656, http://dx.doi.org/10.1126/science.1251682, https://science.sciencemag.org/content/345/6197/653.
- [4] J. Chapman, P. Batson, E. Waddell, R. Ferrier, The direct determination of magnetic domain wall profiles by differential phase contrast electron microscopy, Ultramicroscopy 3 (1978) 203–214, http://dx.doi.org/10. 1016/S0304-3991(78)80027-8, https://www.sciencedirect.com/science/article/ pii/S0304399178800278.
- [5] K.X. Nguyen, X.S. Zhang, E. Turgut, M.C. Cao, J. Glaser, Z. Chen, M.J. Stolt, C.S. Chang, Y.-T. Shao, S. Jin, G.D. Fuchs, D.A. Muller, Disentangling magnetic and grain contrast in polycrystalline FeGe thin films using four-dimensional Lorentz scanning transmission electron microscopy, Phys. Rev. Appl. 17 (2022) 034066, http://dx.doi.org/10.1103/PhysRevApplied.17.034066, https://link.aps.org/doi/10.1103/PhysRevApplied.17.034066.
- [6] F. Krizek, S. Reimers, Z. Kašpar, A. Marmodoro, J. Michalička, O. Man, A. Edström, O.J. Amin, K.W. Edmonds, R.P. Campion, F. Maccherozzi, S.S. Dhesi, J. Zubáč, D. Kriegner, D. Carbone, J. Železný, K. Výborný, K. Olejník, V. Novák, J. Rusz, J.-C. Idrobo, P. Wadley, T. Jungwirth, Atomically sharp domain walls an antiferromagnet, Sci. Adv. 8 (13) (2022) eabn3535, http://dx.doi.org/10.1126/sciadv.abn3535, https://www.science.org/doi/abs/10.1126/sciadv.abn3535.
- [7] Y. Kohno, T. Seki, S.D. Findlay, Y. Ikuhara, N. Shibata, Real-space visualization of intrinsic magnetic fields of an antiferromagnet, Nature 602 (7896) (2022) 234–239, http://dx.doi.org/10.1038/s41586-021-04254-z, https://www.nature. com/articles/s41586-021-04254-z.
- [8] K. Hisao, A. Norio, The magnetic structure of Fe<sub>2</sub>As, J. Phys. Soc. Japan 21 (11) (1966) 2238–2243, http://dx.doi.org/10.1143/JPSJ.21.2238.
- [9] K. Yang, K. Kang, Z. Diao, A. Ramanathan, M.H. Karigerasi, D.P. Shoemaker, A. Schleife, D.G. Cahill, Magneto-optic response of the metallic antiferromagnet Fe<sub>2</sub>As to ultrafast temperature excursions, Phys. Rev. Mater. 3 (2019) 124408, http://dx.doi.org/10.1103/PhysRevMaterials.3.124408, https://link.aps.org/doi/ 10.1103/PhysRevMaterials.3.124408.
- [10] J.C. Loudon, Antiferromagnetism in NiO observed by transmission electron diffraction, Phys. Rev. Lett. 109 (2012) 267204, http://dx.doi.org/10.1103/ PhysRevLett.109.267204, https://link.aps.org/doi/10.1103/PhysRevLett.109. 267204.
- [11] A.K. Yadav, K.X. Nguyen, Z. Hong, P. García-Fernández, P. Aguado-Puente, C.T. Nelson, S. Das, B. Prasad, D. Kwon, S. Cheema, A.I. Khan, C. Hu, J. Íñiguez, J. Junquera, L.-Q. Chen, D.A. Muller, R. Ramesh, S. Salahuddin, Spatially resolved steady-state negative capacitance, Nature 565 (7740) (2019) 468–471, http://dx.doi.org/10.1038/s41586-018-0855-y.
- [12] K. Moore, U. Bangert, M. Conroy, Aberration corrected STEM techniques to investigate polarization in ferroelectric domain walls and vortices, APL Mater. 9 (2) (2021) 020703, http://dx.doi.org/10.1063/5.0035958.
- [13] C. Ophus, Four-dimensional scanning transmission electron microscopy (4D-STEM): From scanning nanodiffraction to ptychography and beyond, Microsc. Microanal. 25 (3) (2019) 563–582, http://dx.doi.org/10.1017/ S1431927619000497.
- [14] M.W. Tate, P. Purohit, D. Chamberlain, K.X. Nguyen, R. Hovden, C.S. Chang, P. Deb, E. Turgut, J.T. Heron, D.G. Schlom, et al., High dynamic range pixel array detector for scanning transmission electron microscopy, Microsc. Microanal. 22 (1) (2016) 237–249, http://dx.doi.org/10.1017/S1431927615015664.
- [15] K. Yang, K. Kang, Z. Diao, M.H. Karigerasi, D.P. Shoemaker, A. Schleife, D.G. Cahill, Magnetocrystalline anisotropy of the easy-plane metallic antiferromagnet Fe<sub>2</sub>As, Phys. Rev. B 102 (2020) 064415, http://dx.doi.org/10.1103/PhysRevB. 102.064415, https://link.aps.org/doi/10.1103/PhysRevB.102.064415.
- [16] K. Müller, F.F. Krause, A. Béché, M. Schowalter, V. Galioit, S. Löffler, J. Verbeeck, J. Zweck, P. Schattschneider, A. Rosenauer, Atomic electric fields revealed by a quantum mechanical approach to electron picodiffraction, Nature Commun. 5 (2014) 1–8, http://dx.doi.org/10.1038/ncomms6653.

- [17] M.C. Cao, Y. Han, Z. Chen, Y. Jiang, K.X. Nguyen, E. Turgut, G.D. Fuchs, D.A. Muller, Theory and practice of electron diffraction from single atoms and extended objects using an EMPAD, Microscopy 67 (December 2017) (2018) i150-i161, http://dx.doi.org/10.1093/jmicro/dfx123.
- [18] J.M. Cowley, A.F. Moodie, The scattering of electrons by atoms and crystals. I. A new theoretical approach, Acta Crystallogr. 10 (10) (1957) 609–619, http://dx.doi.org/10.1107/s0365110x57002194.
- [19] A. Rother, K. Scheerschmidt, Relativistic effects in elastic scattering of electrons in TEM, Ultramicroscopy 109 (2) (2009) 154–160, http://dx.doi.org/10.1016/j. ultramic.2008.08.08.
- [20] V. Grillo, L. Marrucci, E. Karimi, R. Zanella, E. Santamato, Quantum simulation of a spin polarization device in an electron microscope, New J. Phys. 15 (2013) http://dx.doi.org/10.1088/1367-2630/15/9/093026.
- [21] A. Edström, A. Lubk, J. Rusz, Elastic scattering of electron vortex beams in magnetic matter, Phys. Rev. Lett. 116 (12) (2016) 1–5, http://dx.doi.org/10. 1103/PhysRevLett.116.127203.

- [22] A. Edström, A. Lubk, J. Rusz, Quantum mechanical treatment of atomic-resolution differential phase contrast imaging of magnetic materials, Phys. Rev. B 99 (2019) 174428, https://dx.doi.org/10.1103/PhysRevB.99.174428, https://link.aps.org/doi/10.1103/PhysRevB.99.174428.
- [23] E.J. Kirkland, Advanced Computing in Electron Microscopy, Springer US, Boston, MA, 2010, http://dx.doi.org/10.1007/978-1-4419-6533-2, http://link.springer.com/10.1007/978-1-4419-6533-2.
- [24] E.J. Kirkland, Advanced Computing in Electron Microscopy, Springer US, Boston, MA, 2010, pp. 183–184, http://dx.doi.org/10.1007/978-1-4419-6533-2, Ch. 7. http://link.springer.com/10.1007/978-1-4419-6533-2.
- [25] K. Kunc, Recent results in semiconductor dynamics by Ab Initio 'Direct' approach, in: Electronic Structure, Dynamics, and Quantum Structural Properties of Condensed Matter, Springer US, Boston, MA, 1985, pp. 227–312, http://dx.doi.org/10.1007/978-1-4757-0899-8\_6, http://link.springer.com/10.1007/978-1-4757-0899-8\_6.